7. Perovic, A. & Murti, D. K. The effect of coatings on the surface precipitation of oligomeric crystals in poly(ethylene terephthalate) films. *J. Appl. Polym. Sci.* **29** Part 2, 4321–4327 (1984).
8. Needles, H. L., Berns, R. S., Lu, W. C., Alger, K. & Varma, D. S. Effect of nonionic surfactant and heat on selected properties on polyester. *J. Appl. Polym. Sci.* **25,** 1737–1744 (1980).
9. Perovic, A. & Sundararajan, P. R. Crystallization of cyclic oligomers in commercial poly(ethylene terephthalate) films. *Polym. Bull.* **6,** 277–283 (1982).
10. Neubrand, A. & Rodel, J. Gradient materials: An overview of a novel concept. *Z. Metallkd.* **88,** 358–371 (1997).
11. Gladden, L. F. *et al.* Structural studies of high surface area silicas. *J. Non-Cryst. Solids* **139,** 47–59 (1992).
12. Dariel, M. P., Levin, L. & Frage, N. Graded ceramic preforms: Various proceeding approaches. *Mater. Chem. Phys.* **67,** 192–198 (2001).
13. Fischbach, D. B. & Lemoine, P. M. Influence of a CVD carbon coating on the mechanical property stability of nicalon silicon carbide fibre. *Composites Sci. Technol.* **37,** 55–61 (1990).
14. Li, J. X., Matsuo, Y. & Kimura, S. Improvement of thermal stability of SiC fibre by CVD-C.SiC coating. *Bull. Ceram. Soc. Jpn* **99,** 1207–1211 (1991).
15. Moya, J. S., Sanchez-Herencia, M. R., Pena, P. & Requena, J. Layered ceramic composites: A new family of advanced materials. *Third Euro-Ceramics* (eds Durán, P. & Fenández, J. F.) **3,** 289–300 (Feenza Editrica Iberica, Spain, 1993).
16. Sidky, P. S. & Hocking, M. G. Review of inorganic coatings and coating processes for reducing wear and corrosion. *Br. Corrosion J.* **34,** 171–183 (1999).
17. Somiya, S. (ed.) *Hydrothermal Reactions for Materials Science and Engineering* (Elsevier, London, 1989).
18. Varaprasad, D. V., Wade, B., Venkatasubramanian, N., Desai, P. & Abhiraman, A. S. Critical requirements in the formation of continuous ceramic fibre precursors. *Ind. J. Fibre Textile Res.* **16,** 73–82 (1991).
19. Bhat, D. G., Rebenne, H. E. & Strandberg, C. Analysis of coating interlayer between silicon nitride cutting tools and titanium carbide and titanium nitride coatings. *J. Mater. Sci.* **26,** 4567–4580 (1991).
20. Takeda, M., Sakamoto, J., Saeki, A., Imai, Y. & Ichikawa, H. High performance silicon carbide fibre Hi-Nicalon for ceramic matrix composites. *Ceram. Eng. Sci. Proc.* **16,** 37–44 (1995).
21. Ishikawa, T., Kohtoku, Y., Kumagawa, K., Yamamura, T. & Nagasawa, T. High-strength alkali-resistant sintered SiC fibre stable to 2,200 °C. *Nature* **391,** 773–775 (1998).
22. Yamaoka, H., Harada, Y. & Fujii, T. Inorganic fibre including zirconia and its production process. Japanese patent Application No. 2001-167679 (2001).
23. Abe, Y., Gunji, T. & Hikita, M. Preparation of SiO_2-TiO_2 fibres from polytitanosiloxanes. *Yogyokyokai-shi* **94** (12), 1243–1245 (1986).
24. Shen, L., Tan, B. J., Willis, W. S., Galasso, F. S. & Suib, S. L. Characterization of dip-coated boron nitride on silicon carbide fibres. *J. Am. Ceram. Soc.* **77,** 1011–1016 (1994).

Competing interests statement

The authors declare that they have no competing financial interests.

Correspondence and requests for materials should be addressed to T.I. (e-mail: 24613u@ube-ind.co.jp).

Observation and interpretation of a time-delayed mechanism in the hydrogen exchange reaction

Stuart C. Althorpe*†, Félix Fernández-Alonso‡, Brian D. Bean§, James D. Ayers§, Andrew E. Pomerantz§, Richard N. Zare§ & Eckart Wrede*

** Department of Chemistry, University of Durham, Durham DH1 3LE, UK*
‡ Istituto di Struttura della Materia – Consiglio Nazionale delle Ricerche, Area della Ricerca di Roma – Tor Vergata, via del Fosso del Cavaliere 100, 00133 Rome, Italy
§ Department of Chemistry, Stanford University, Stanford, California 94305-5080, USA

Extensive theoretical[1–13] and experimental[2,13–22] studies have shown the hydrogen exchange reaction $H + H_2 \rightarrow H_2 + H$ to occur predominantly through a 'direct recoil' mechanism: the H–H bonds break and form concertedly while the system passes straight over a collinear transition state, with recoil from the collision causing the H_2 product molecules to scatter backward. Theoretical predictions agree well with experimental observations of this scattering process[15–20,22]. Indirect exchange mechanisms involving H_3 intermediates have been suggested to occur as well[8–13], but these are difficult to test because bimolecular reactions cannot be studied by the femtosecond spectroscopies[23] used to monitor unimolecular reactions. Moreover, full quantum simulations of the time evolution of bimolecular reactions have not been performed. For the isotopic variant of the hydrogen exchange reaction, $H + D_2 \rightarrow HD + D$, forward scattering features[21] observed in the product angular distribution have been attributed[21,12] to possible scattering resonances associated with a quasibound collision complex. Here we extend these measurements to a wide range of collision energies and interpret the results using a full time-dependent quantum simulation of the reaction, thus showing that two different reaction mechanisms modulate the measured product angular distribution features. One of the mechanisms is direct and leads to backward scattering, the other is indirect and leads to forward scattering after a delay of about 25 femtoseconds.

The dominant recoil mechanism in the $H + H_2$ reaction may be written as

$$H\text{–}H \leftarrow H \Rightarrow \leftarrow H\text{—}H \leftarrow H \Rightarrow \leftarrow H\ H\text{–}H \rightarrow \qquad (1)$$

where the arrows indicate the direction of motion of the species involved. This mechanism results in 'backward scattered' H_2 angular distributions, which recoil from the collision at centre-of-mass scattering angles θ close to 180° (where θ is measured from the approach direction of the H reagent at $\theta = 0°$). A recent *ab initio* potential energy surface for this system, the BKMP2 surface[4], is so accurate that the theoretical angular distributions, obtained by solving the exact time-independent Schrödinger equation for motion of the H atoms on this surface, are in excellent quantitative agreement with experiment[15–20,22].

Quasiclassical[8,21] and quantum[9] calculations have also predicted ridge structures along a line in the energy–angle (E–θ) plane which evolve into broad peaks in the 'forward direction' (around $\theta = 0°$). The quasiclassical ridges were associated with a time-delayed (15–35 fs) mechanism, although this classical prediction should be interpreted with care because the quasiclassical method does not give an exact description of the scattering dynamics. The quasiclassical[8] E–θ ridges and forward scattering features are less pronounced than their quantum[9] counterparts, indicating that quantum effects are important in causing these phenomena. In the isotopic variant of the hydrogen exchange reaction, $H + D_2 \rightarrow HD(v' = 3, j' = 0) + D$, forward scattering[21] has been observed at a collision energy $E = 1.64$ eV (v' and j' refer to the vibrational and rotational quantum numbers of the diatomic product, respectively). For $HD(v' = 3, j' = 0)$, the quasiclassical calculations underestimated the amount of forward scattering by about a factor of three[21], while model quantum calculations[12] indicated that a quantum threshold resonance, associated with a quasibound complex formed by the collision partners, was possible at this energy.

The experiments reported here used the PHOTOLOC (photo-initiated reaction analysed via the law of cosines) technique[17,18,21,22]. A 1:9 mixture of HBr and D_2 is expanded in a free jet using a pulsed nozzle valve. The reaction is initiated by photolysing HBr with a 5-ns laser pulse, varying the photolysis wavelength between 203 and 225 nm to correspond to the nine collision energies shown in Fig. 1. The $HD(v' = 3, j' = 0)$ product is detected 15 ns after photoinitiation, using (2+1) resonance enhanced multiphoton ionization (REMPI) through the Q-branch members of the HD EF $^1\Sigma_g^+$–X $^1\Sigma_g^+$ (0,3) band[24]. The energy resolution of the experiment is about 50 meV full-width at half-maximum, due mainly to the residual translational temperature ($T \approx 50$ K) of the beam expansion.

A direct comparison of the experimental measurements with the theoretical predictions is presented in Fig. 1 in the form of time-of-flight (TOF) profiles of the $HD(v' = 3, j' = 0)$ product. The theoretical TOF profiles were calculated by solving the exact time-dependent Schrödinger equation for the $H + D_2(v = 0, j = 0)$ reaction on the BKMP2 potential energy surface[4], using a recently developed

† Present address: School of Chemistry, University of Exeter, Stocker Road, Exeter EX4 4QD, UK.

wavepacket method[25], extended as explained below. Angular distributions, at fixed values of E from 1.3 to 2.2 eV, were calculated by summing all partial waves from total angular momentum $J = 0$ to 30, and were converged to better than 2%. The convergence of selected fixed-J reaction probabilities was checked by comparing with results calculated using the CCP6 time-independent code[26]. The calculated angular distributions were then convoluted with the instrumental and collision-energy resolution of the experiment to obtain the TOF profiles shown in Fig. 1.

The experimental and theoretical TOF profiles in Fig. 1 are in excellent agreement. The most notable feature in the TOF profiles is the overall change in shape as a function of collision energy, which we interpret by referring to the calculated HD($v' = 3,j' = 0$) angular distributions as a function of collision energy in Fig. 2. (Strictly speaking Fig. 2 shows the angular distributions multiplied by a factor of sinθ, so as to give a fair representation of the amount of reaction product per solid angle.) On passing from a collision energy of 1.5 eV to 1.8 eV, the angular distribution changes from being mainly sideways scattered to being (asymmetrically) forward–backward peaked. This change maps onto the TOF profiles as a change from a broad pair of peaks around ±25 ns, at 1.5 eV, to three narrow peaks around 0 ns and ±50 ns, at 1.8 eV. The ±25-ns peaks correspond to sideways scattering in Fig. 2, the 0-ns peak to back scattering, and the ±50-ns side peaks to forward scattering. Note that the reduction in height of the ±50-ns peaks between 1.64 and 1.85 eV is caused by a reduction in experimental sensitivity to forward-scattering features—not by a reduction in the forward scattering itself. The forward scattering remains strong between 1.64 and 1.85 eV while becoming narrower. This feature is the onset of a broad forward scattering peak as a function of collision energy, such as predicted previously for the H + H_2 (ref. 9) and D + H_2 (refs 8 and 9) reactions at lower collision energies. Our TOF profiles are, to our knowledge, the first experimental measurement of this feature, and also of the E–θ 'ridge', which, for H + D_2 → HD($v' = 3,j' = 0$) + D,

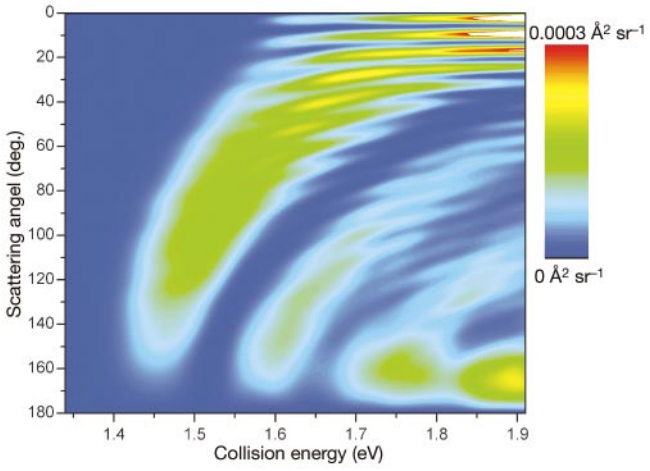

Figure 2 Calculated HD($v' = 3,j' = 0$) angular distributions. The distributions [d$\sigma(E,\theta)$/dΩsinθ)] are plotted as a function of collision energy E and centre-of-mass scattering angle θ. The forward ($\theta \approx 0°$) peak at $E > 1.6$ eV shows up as the side-peaks at ±50 ns in the TOF profiles of Fig. 1. The ridge between collision energies of 1.4 and 1.7 eV causes the broadening of the TOF profiles between collision energies of 1.39 to 1.64 eV.

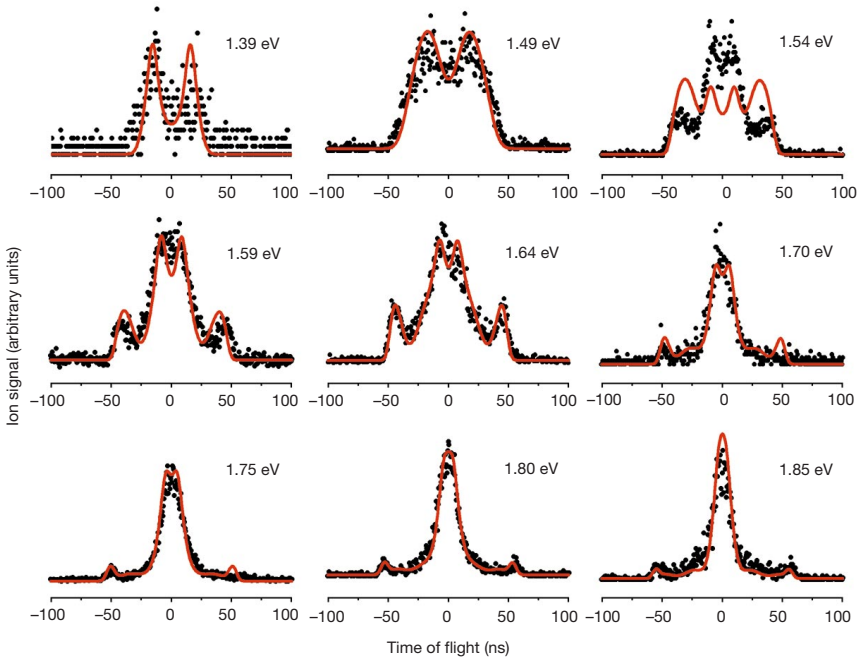

Figure 1 Comparison between experimental and theoretical results for the H + D_2 → HD($v' = 3,j' = 0$) + D reaction. Each frame is a plot of an experimental (black dots) and theoretical (red curve) time-of-flight (TOF) profile, showing the number of ionized HD($v' = 3,j' = 0$) molecules that arrive at the detector as a function of time. There is a one-to-one mapping between this arrival time (which should not be confused with the time t used to follow the reaction mechanism in Fig. 3) and the centre-of-mass scattering angle θ (measured from the approach direction of the H reagent at $\theta = 0°$). Each black dot represents the total HD($v' = 3,j' = 0$) single-ion count at a given time of arrival at the detector. The spread in the experimental points is indicative of the statistical errors arising from the Poisson-like statistics of the ion-counted signals. Systematic errors were identified and reduced to a minimum by performing at least three independent measurements of the same TOF profile at each collision energy. The TOF profiles are symmetric about the centre because there are as many reagent H atoms with speed projections towards the detector as those away from the detector. The theoretical TOF profiles were obtained by convoluting the calculated angular distributions of Fig. 2 with the instrumental and collision-energy resolution of the experiment. At present we do not understand the cause of the discrepancies at 1.54 eV, although we note that it is around this energy that the shape of the angular distributions changes most rapidly as a function of collision energy; also, the calculations included only the lowest rotational level of the D_2($v = 0$) reagent, whereas higher rotational levels ($j < 3$) contribute to the experimental signal. The excellent overall agreement between theory and experiment means that the simulation shown in Fig. 3 is a realistic picture of the reaction mechanism.

lies between 1.4 and 1.7 eV (see Fig. 2). As E increases from 1.4 to 1.7 eV, the ridge moves in the forward direction, evolving into the forward peak. Hence the scattering features predicted previously[8,9] and attributed to indirect processes are responsible for the overall change in the shape of the TOF profiles.

The excellent agreement between experiment and theory suggests that the wavefunction we use provides a realistic description of the motion of the atoms during the reaction. To obtain the time-dependent wavefunction, we built on previous work[27–29] on calculating time-dependent wavefunctions for fixed values of J (usually $J = 0$). We extend the method of ref. 25 to calculate the fixed-J wavefunctions for every value of J that contributes to the angular distributions (that is, $J = 0$–30). The fixed-J wavefunctions are then superposed to give the complete wavefunction, Ψ, which describes the motion of the nuclei as a function of time, t, and of the six coordinates that locate the nuclei in the centre-of-mass frame. We next project Ψ onto the HD($v' = 3$, $j' = 0$) rovibrational product state, obtaining the function $\Phi(R,\theta,t)$ which describes when and where the HD($v' = 3$,$j' = 0$) product is formed, and how it scatters. Note that R is the distance from the product HD centre of mass to the product D atom, and θ is the centre-of-mass scattering angle defined above.

We calculate $|\Phi(R,\theta,t)|^2 \sin\theta$ at 120 values of t from 0 to 100 fs. Plots at selected values of t are shown in blue in Fig. 3. The symmetry about the H–DD approach axis reflects the cylindrical symmetry of the reaction in three-dimensional space, which is ensured at $t = 0$ by the symmetry of the $D_2(v = 0,j = 0)$ wavefunction, and is preserved throughout the collision. The spatial part of Ψ at time $t = 0$ is a plane-wave wavepacket $\chi(R',\theta')$, which describes the H atom approaching $D_2(v = 0,j = 0)$ from a mean separation R' of 6 bohr (where (R',θ') are the reagent analogues to (R,θ)). The function $|\chi(R',\theta')|^2$ is plotted in green in Fig. 3. Note that $\chi(R',\theta')$ is made up of a superposition of time-independent wavefunctions, describing the H–DD approach motion over a continuous range of collision energies from 1.33 to 2.2 eV. The distribution of these energies is flat, damping to zero at the edges. (The precise form of the distribution is a Fourier-transformed distributed approximating functional[30], centred about 1.65 eV, with σ and M (defined in ref. 30) set to 0.07 eV and 88.) Using different energy distributions confirmed that all the key features in Fig. 3 were independent of the form of the energy distribution.

Figure 3 demonstrates that the HD($v' = 3$,$j' = 0$) product is formed by two distinct reaction mechanisms. The first mechanism is the recoil mechanism of equation (1), which ejects the HD product in the opposite direction to the H–DD approach direction. The second mechanism occurs roughly 25 fs after the recoil mechanism, and ejects most of the HD product in the opposite (forward) direction. This time-delayed mechanism causes the broad

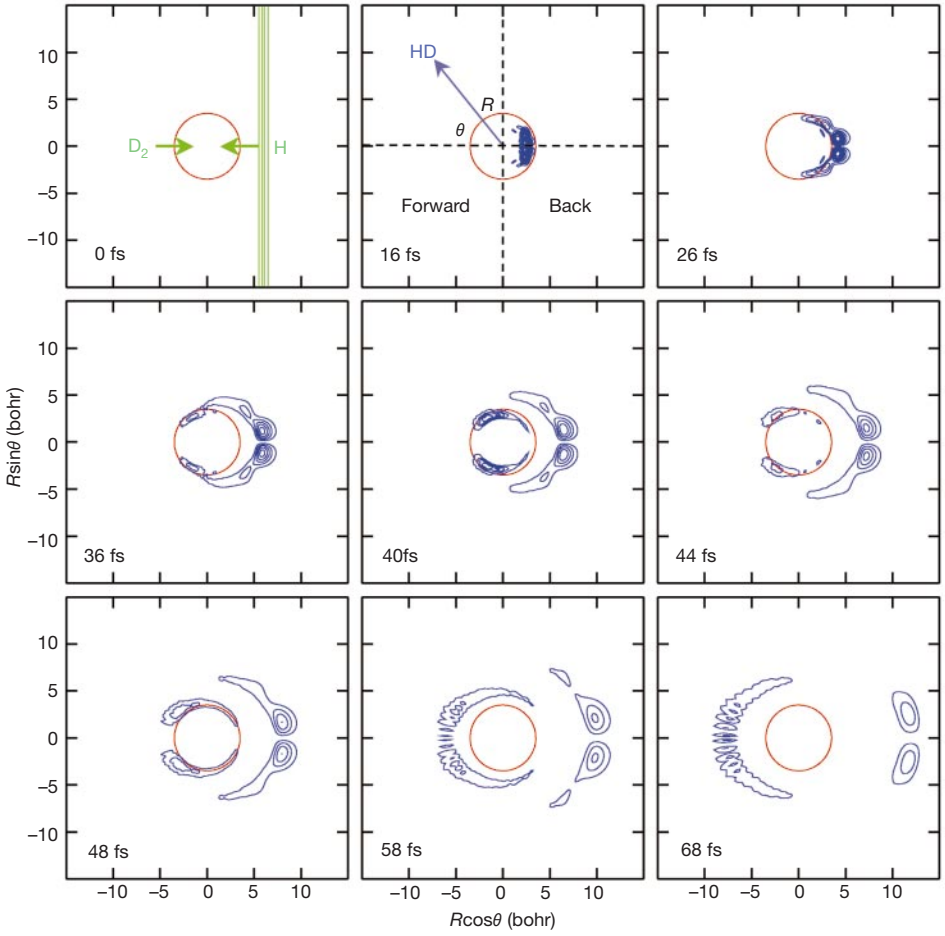

Figure 3 Snapshots from the quantum simulation of the H + $D_2(v = 0,j = 0)$ ⟶ HD($v' = 3,j' = 0$) + D reaction. The blue contours are obtained from the complete wavefunction of the reaction as explained in the text, and show the time-evolution of the HD($v' = 3,j' = 0$) product, as a function of the centre-of-mass scattering angles R and θ. The green contours and arrows show the location and direction of travel of the reagents at $t = 0$. The red circles are of radius $R = 3.5$ bohr and give a rough indication of the extent of the transition state region. Two reaction mechanisms are visible, separated by a time delay of about 25 fs. The earlier mechanism, which throws out most of its products in the backward direction, is the direct 'recoil' mechanism, and is responsible for the central peaks in the TOF profiles of Fig. 1. The time-delayed mechanism, which throws out most of its products in the forward direction, is responsible for the side peaks in the TOF profiles of Fig. 1. Snapshots are shown here for selected values of t; the entire sequence of frames is available as a movie (at http://www.dur.ac.uk/chemistry/publications/sc_althorpe/nature.html).

forward peak in Fig. 2, and hence the side peaks in the TOF profiles in Fig. 1. Analysis of the angular distributions showed that the time-delayed mechanism is also mainly responsible for the sideways ridge (see Fig. 2), and hence for the broadening of the TOF profiles around $E = 1.4–1.7$ eV.

We see that the HD product from the time-delayed mechanism starts to form at scattering angles of roughly 45°, where the wavefunction is found to have mostly 'high impact parameter' components, corresponding to $J = 15–20$. This indicates that the H atoms that react via this mechanism come from the parts of the plane wave (green function in Fig. 3) around $R\sin\theta = \pm(1.1–1.6)$ bohr. It is likely therefore that H attacks the D_2 at a glancing angle, in contrast to the direct mechanism (in which H attacks the D_2 bond collinearly). If this happens, then energy initially concentrated in the HDD bend must be converted into energy along the HDD asymmetric stretch, to allow the system to pass over the transition state and react.

The successful combination of experiment and theory to elucidate in detail the mechanisms involved in one of the simplest chemical reactions, the hydrogen exchange reaction, can also be applied to more complex reactions. These include the reactions $O(^1D) + H_2 \rightarrow OH + H$, $F + HD \rightarrow HF + D$, and $H + H_2O \rightarrow OH + H_2$, for which experimental angular distributions and realistic potential energy surfaces are available[19,20], and for which it is computationally feasible to solve the time-dependent Schrödinger equation. □

Received 24 October 2001; accepted 22 January 2002.

1. Hirshfelder, J. O., Eyring, H. & Topley, B. Reactions involving hydrogen molecules and atoms. *J. Chem. Phys.* **4,** 170–177 (1936).
2. Truhlar, D. G. & Wyatt, R. E. History of H_3 kinetics. *Annu. Rev. Phys. Chem.* **27,** 1–43 (1976).
3. Neuhauser, D. *et al.* State-to-state rates for the $D + H_2(v = 1, j = 1) \rightarrow HD(v', j') + H$ reaction–predictions and measurements. *Science* **257,** 519–522 (1992).
4. Boothroyd, A. I., Keogh, W. J., Martin, P. G. & Peterson, M. R. A refined H_3 potential surface. *J. Chem. Phys.* **104,** 7139–7152 (1996).
5. Zhang, J. Z. H. & Miller, W. H. Quantum reactive scattering via the S-matrix version of the Kohn variational principle: integral cross sections for $H + H_2(v_1 = j_1 = 0) \rightarrow H_2(v_2 = 1, j_2 = 1,3) + H$ in the energy range $E_{total} = 0.9$-1.4 eV. *Chem. Phys. Lett.* **153,** 465–470 (1988).
6. Miller, W. H. Recent advances in quantum mechanical reactive scattering theory. *Annu. Rev. Phys. Chem.* **41,** 245–281 (1990).
7. D'Mello, M., Manolopoulos, D. E. & Wyatt, R. E. Quantum dynamics of the $H + D_2 \rightarrow D + HD$ reaction: comparison with experiment. *J. Chem. Phys.* **94,** 5985–5993 (1991).
8. Aoiz, F. J., Herrero, V. J. & Sáez Rábanos, V. Quasiclassical state to state reaction cross sections for $D + H_2(v = 0, j = 0) \rightarrow HD(v', j') + H$. Formation and characteristics of short-lived collision complexes. *J. Chem. Phys.* **97,** 7423–7436 (1992).
9. Miller, W. H. & Zhang, J. Z. H. How to observe the elusive resonances in H or $D + H_2 \rightarrow H_2$ or HD + H reactive scattering. *J. Phys. Chem.* **95,** 12–19 (1991).
10. Schatz, G. C. & Kuppermann, A. Dynamical resonances in collinear, coplanar, and three-dimensional quantum mechanical reactive scattering. *Phys. Rev. Lett.* **35,** 1266–1269 (1973).
11. Skodje, R. T., Sadeghi, R., Köppel, H. & Krause, J. L. Spectral quantization of transition state dynamics for the three-dimensional $H + H_2$ reaction. *J. Chem. Phys.* **101,** 1725–1729 (1994).
12. Allison, T. C., Friedman, R. S., Kaufman, D. J. & Truhlar, D. G. Analysis of the resonance in $H + D_2 \rightarrow HD(v' = 3) + D$. *Chem. Phys. Lett.* **327,** 439–445 (2000).
13. Fernández-Alonso, F. & Zare, R. N. Scattering resonances in the simplest chemical reaction. *Annu. Rev. Phys. Chem.* **53,** 67–99 (2002).
14. Nieh, J.-C. & Valentini, J. J. Experimental observation of dynamical resonances in the $H + H_2$ reaction. *Phys. Rev. Lett.* **60,** 519–522 (1988).
15. Schnieder, L., Seekamp-Rahn, K., Wrede, E. & Welge, K. H. Experimental determination of quantum state resolved differential cross sections for the hydrogen exchange reaction $H + D_2 \rightarrow HD + D$. *J. Chem. Phys.* **107,** 6175–6195 (1997).
16. Wrede, E. *et al.* The dynamics of the hydrogen exchange reaction at 2.20 eV collision energy: comparison of experimental and theoretical differential cross sections. *J. Chem. Phys.* **110,** 9971–9981 (1999).
17. Fernández-Alonso, F., Bean, B. D. & Zare, R. N. Differential cross sections for $H + D_2 \rightarrow HD(v' = 1, J' = 1,5,8) + D$ at 1.7 eV. *J. Chem. Phys.* **111,** 1035–1042 (1999).
18. Fernández-Alonso, F., Bean, B. D. & Zare, R. N. Differential cross sections for $H + D_2 \rightarrow HD(v' = 2, J' = 0,3,5) + D$ at 1.55 eV. *J. Chem. Phys.* **111,** 2490–2498 (1999).
19. Liu, K. Crossed-beam studies of neutral reactions: state-specific differential cross sections. *Annu. Rev. Phys. Chem.* **52,** 139–164 (2001).
20. Casavecchia, P. Chemical reaction dynamics with molecular beams. *Rep. Prog. Phys.* **63,** 355–414 (2000).
21. Fernández-Alonso, F. *et al.* Evidence for scattering resonances in the $H + D_2$ reaction. *Angew. Chem. Int. Edn Engl.* **39,** 2748–2752 (2000).
22. Fernández-Alonso, F. *et al.* Forward scattering in the $H + D_2 \rightarrow HD + D$ reaction: comparison between experiment and theoretical predictions. *J. Chem. Phys.* **115,** 4534–4545 (2001).
23. Zewail, A. H. Femtochemistry: atomic-scale dynamics of the chemical bond. *J. Phys. Chem.* **104,** 5660–5694 (2000).
24. Rinnen, K.-D., Buntine, M. A., Kliner, D. A. V., Zare, R. N. & Huo, W. M. Quantitative determination of H_2, HD, and D_2 internal-state distributions by (2+1) resonance-enhanced multiphoton ionization. *J. Chem. Phys.* **95,** 214–225 (1991).
25. Althorpe, S. C. Quantum wavepacket method for state-to-state reactive cross sections. *J. Chem. Phys.* **114,** 1601–1616 (2001).
26. Skouteris, D., Castillo, J. F. & Manolopoulos, D. E. ABC: a quantum reactive scattering program. *Comput. Phys. Commun.* **133,** 128–135 (2000).
27. Althorpe, S. C., Kouri, D. J. & Hoffman, D. K. Further partitioning of the reactant-product decoupling equations of state-to-state reactive scattering and their solution by the time-independent wavepacket method. *J. Chem. Phys.* **107,** 7816–7824 (1997).
28. Judson, R. S., Kouri, D. J., Neuhauser, D. & Baer, M. Time-dependent wavepacket method for the complete determination of S-matrix elements for reactive molecular collisions in 3 dimensions. *Phys. Rev. A* **42,** 351–366 (1990).
29. Balint-Kurti, G. G., González, A. I., Goldfield, E. M. & Gray, S. K. Quantum reactive scattering of $O(^1D) + H_2$ and $O(^1D) + HD$. *Faraday Discuss.* **110,** 169–183 (1998).
30. Huang, Y., Zhu, W., Kouri, D. J. & Hoffman, D. K. Distributed approximating function approach to atom-diatom reactive scattering: Time-dependent and time-independent wavepacket treatments. *J. Phys. Chem.* **98,** 1868–1874 (1994).

Acknowledgements

We thank L. Bañares and J. F. Castillo for discussions on the $H + D_2$ reaction, and D. C. Clary, D. E. Manolopoulos and J. M. Hutson for reading the manuscript. S.C.A. thanks the Royal Society for a University Research Fellowship. F.F.A. acknowledges partial support by a European Union Marie Curie fellowship. The experimental part of this work was supported at Stanford by the US National Science Foundation.

Competing interests statement

The authors declare that they have no competing financial interests.

Correspondence and requests for materials should be addressed to S.C.A. (e-mail: s.c.althorpe@ex.ac.uk).

Glacial–interglacial stability of ocean pH inferred from foraminifer dissolution rates

David M. Anderson* & David Archer†

* *NOAA Paleoclimatology Program and University of Colorado, 325 Broadway, Boulder, Colorado 80303, USA*

† *Department of Geophysical Sciences, University of Chicago, 5734 S. Ellis Ave., Chicago, Illinois 60637, USA*

The pH of the ocean is controlled by the chemistry of calcium carbonate. This system in turn plays a large role in regulating the CO_2 concentration of the atmosphere on timescales of thousands of years and longer. Reconstructions of ocean pH and carbonate-ion concentration are therefore needed to understand the ocean's role in the global carbon cycle. During the Last Glacial Maximum (LGM), the pH of the whole ocean is thought to have been significantly more basic[1], as inferred from the isotopic composition of boron incorporated into calcium carbonate shells, which would partially explain the lower atmospheric CO_2 concentration at that time. Here we reconstruct carbonate-ion concentration—and hence pH—of the glacial oceans, using the extent of calcium carbonate dissolution observed in foraminifer faunal assemblages as compiled in the extensive global CLIMAP data set[2]. We observe decreased carbonate-ion concentrations in the glacial Atlantic Ocean, by roughly 20 μmol kg^{-1}, while little change occurred in the Indian and Pacific oceans relative to today. In the Pacific Ocean, a small (5 μmol kg^{-1}) increase occurred below 3,000 m. This rearrangement of ocean pH may be due to changing ocean circulation from glacial to present times, but overall we see no evidence for a shift in the whole-ocean pH as previously inferred from boron isotopes[1].